

Analysis of Influence of Vertical Vibration on Natural Heat Convection Coefficients from Horizontal Concentric and Eccentric Annulus

Baydaa Khalil Khudhair*, Adel Mahmood Saleh and Ali Laftah Ekaid

University of Technology, Mechanical Engineering Department, Baghdad 00964, Iraq

ABSTRACT

The research looks at how heat transmission is improved when two horizontal cylinders are concentric or vertically eccentric, creating vertical motion. The inner cylinder is uniformly heated, whereas the outer cylinder is isothermal. Apart from Rayleigh's number ($10^2 \geq Ra \geq 10^6$), eccentricity (normalized by the radius difference) at range ($\epsilon = 0, \pm 0.625$ & ± 0.333), and Prandtl number is fixed $Pr = 0.7$ (air), the vibrational frequencies are changed from ($\omega = 0, 100, 1000$ & 10000). The steady-state, two-dimensional Navier-Stokes equations (with Boussineq approximation) are generated using central difference approximation and solved using the successive over-relaxation (LSOR) method line by line. The contour maps of streamlines and heat lines clearly illustrate the annuli's heat and fluid flow patterns. According to the results, it is found that the vibration generally enhanced the heat transfer rate more than the stationary one for all values of frequency and different eccentricities with various rates of enhancement. Vibration thermal convection is prominent at low Rayleigh ($Ra = 10^2, 10^3, 10^4$), and the vibration significantly boosts the heat transfer rate within an annular annulus. In a high Rayleigh number situation, a high Rayleigh number situation ($Ra=10^5$ and 10^6), gravitational thermal convection predominates, and vibration motion does not significantly improve heat transmission. The vibration is a powerful augmentation tool for placing the inner cylinder towards the bottom of the outer cylinder (negative

ARTICLE INFO

Article history:

Received: 05 June 2022

Accepted: 04 November 2022

Published: 07 April 2023

DOI: <https://doi.org/10.47836/pjst.31.3.24>

E-mail addresses:

21979@student.uotechnology.edu.iq (Baydaa Khalil Khudhair)

Adel.M.Saleh@uotechnology.edu.iq (Adel Mahmood Saleh)

ali.l.ekaid@uotechnology.edu.iq (Ali Laftah Ekaid)

*Corresponding author

vertical eccentricity ($\epsilon = -0.625$)), the heat rate enhancement more than 3.8-fold at $Ra = 10^3$, $\omega = 10000$. The Nusselt number has been correlated in a dimensionless form as the Rayleigh number and the vibrational Rayleigh number.

Keywords: Cylindrical annulus, heat convection, numerical validation, Rayleigh number, vertical vibration

INTRODUCTION

Predicting heat transfer due to natural (convection and conduction) between eccentric cylinders (horizontal annular fluid layers) has gained substantial attention from researchers in recent decades due to its importance in many engineering applications. Because of the intriguing character of the particular heat transport phenomena and its essential relevance in practical applications, convection in the horizontal annular of concentric and eccentric cylindrical systems has gained substantial weight. Examples of application domains using the horizontal coaxial cylinder geometry investigated in this study include concentrating solar collector receiver design, initial melting of phase change material around heating pipes in thermal storage systems, compressed gas insulated high voltage electric transmission cables, and designing nuclear reactors.

Kuehn and Goldstein (1978) performed a rather extended investigation of instance concentric numerically using the finite difference approach and empirically on the concentric and impact of vertical eccentricity (positive and negative) of the inner cylinder on the local and average heat transfer parameters using Mach-Zehnder techniques; by analyzing this influence with a fixed radius ratio of 2.6 in the boundary layer regime ($3 \times 10^4 < Ra < 5 \times 10^5$). The average heat transfer coefficients were all within 10% of concentric geometry at the boundary layer regime for $\epsilon = \frac{1}{3}, \frac{2}{3}$.

Any thermal device (electronic and thermoelectric) depend upon the feasibility of rejecting waste heat by trouble-free economic methods and, during its normal operation, will encounter some degree of vibration. In particular, the most challenging part of any nonexpendable coolant cooling system, which most rejects heat to the atmosphere, is usually the thermal coupling between the solid convective surface and the cooling air. It is well known that the boundary layers provide the primary resistance to heat flow from the solid surface to the fluid. Therefore, it would seem logical that an approach that could remove the boundary layers would substantially affect the heat flow.

The increasing emergence of diverse technologies worldwide has increased global energy consumption exponentially. A large percentage of this energy is in the form of heat, thus enhancing the heat transfer mechanisms at the forefront of energy transfer and storage.

So, the conceptualized mechanism of vibration breaks through the boundary layer limitation and achieves massive heat transport enhancement. Many vibration and oscillation phenomena occur in the industrial field, like the fluid flow in the medium being subjected to pulsation or agitation (fluid-induced vibration) relative to a stationary cylinder or any other container. The other type of vibration in which the heated body or surface is moved relative to the stationary surrounding fluid of vibration of the mechanical devices has been investigated in studies. Engineering applications of natural convection in eccentric annulus have become of great interest to researchers in recent years. Such a claim arises from eccentricity in mechanical equipment, electrical motors, and generators, which often

cause design tolerance and manufacturing limits. Further applications include drilling and completing an oil well, heat exchanger industries, cooling of the nuclear reactor, and the insulation for burned tubes in district heating and cooling underground electric cables.

Fu and Hung (2006) developed a numerical convection study in a vertical channel flow. According to their theory, a vibrational heat plate with a particular frequency and amplitude combination has less natural convection than an equilibrium point. Alawadhi (2008) investigated the influence of transversely oscillating frequency for the inner cylinder enclosed by an annulus enclosure on the flow fields and thermal behavior. It is concluded that the oscillating frequency of the inner cylinder greatly enhances the average heat transfer rate at the inner cylinder.

Hosseinian et al. (2018) searched experimentally for the enhancement of heat transfer in a flexible double-pipe heat exchanger made of PVDF using MWCNT-water nanofluid as a working fluid. The test rig was examined for different mass fractions, and forced vibration was applied to the outer wall of the heat exchanger generated by electric vibrators. The results showed that using vibration increases the heat transfer rate but simultaneously reduces the deposition of nanoparticles. The increase of many parameters, such as the temperature of nanofluid, vibration level, and mass flow rate, enhances heat transfer. The highest increase in heat transfer coefficient was obtained at the most significant level of vibration ($9 \frac{m}{s}$) and the lowest mass fraction (0.04%).

Nasrat et al. (2019) experimentally studied the effect of transverse vibration on the natural convection heat transfer in a rectangular enclosure with an aspect ratio of 0.5 filled with air as a working fluid aligned horizontally on a mechanical shaker generating a sinusoidal transverse vibrational displacement. Shokouhmand et al. (2011) discovered vortices in test samples' left and right areas due to horizontal vibration, which reduced the heat transmission rate. Furthermore, due to more excellent convective flow crossing cylinders, oscillation had little effect on heat transmission at large Rayleigh numbers. Mahfouz (2012) investigated natural heat convection numerically among two vertical, eccentric, long cylinders inside a circumferential circular pattern. Mahian et al. (2013) conducted a detailed study on a vertical annulus using nanofluids. They demonstrated that frequency magnitude might classify thermal convection into five zones. They also noted that buoyancy-driven thermal convection dominates at a high Rayleigh number ($Ra = 10^6$).

Tayebi et al. (2016) conducted a numerical investigation on natural convection fluid flow and heat transfer in an annulus of two differentially heated eccentric cylindrical ducts filled with the Cu-water nanofluid. A detailed study, including the effects of the mechanical force vibration on the heat transfer characteristics of internal flow in a circular heated tube, has been investigated by Liu et al. (2017). Imtiaz and Mahfouz (2017) used the Fourier Spectral method to examine the impact of thermal boundary conditions on conjugated conduction-free convection heat transfer in an annulus between two concentric cylinders. A

non-Newtonian hybrid nanofluid flowing around a concentric annulus was investigated by Shahsavari et al. (2018) using the Genetic algorithm technique. Using natural convection as a cooling strategy is one of the primary ways to ensure the functional reliability of equipment. The flow characteristics of the annulus are not explored, especially the unsteady flow. It has been investigated theoretically and experimentally how hydrodynamic, and thermal effects interact. Only a handful of studies examined vertical or horizontal eccentricity in their extensive research evaluation (Sarhan et al., 2019).

Ali et al. (2020) presented a 3D simulation of heat transfer (turbulent/laminar) and fluid flow of water through the annulus side of conically tube heat exchangers. Sarhan et al. (2019) proposed a new model to investigate the effect of dynamic response on the thermal stability of a rectangle plate with a constant heating rate. According to test findings, the influence of vibration frequency reached in the horizontal position offered the best performance and maximum heat transfer rate. However, when the plate is vertical, and the vase is flat, the heat transfer rate decreases as the vibration frequency increases. Bouzerzour et al. (2020) achieved a numerical study on natural convection heat transfer and fluid flow in a two-dimensional annulus founded by two differentially heated confocal elliptic cylinders oriented and filled with the water-based silver nanofluid. Wang et al. (2020) presented a numerical and theoretical study of a thermal vibrational turbulence technique that overcomes the constraints of the boundary layer and gains massive heat transport augmentation. Thermal turbulence was a powerful way for the fluid to transport heat through space. However, the presence boundary layer near the surfaces trapped the heat exchanged capacity. As a horizontal vibration was applied to the convection sample, a strong shear was induced to the fluid near the conducting surfaces, destabilizing thermal boundary layers, vigorously triggering thermal plume eruptions, and resulting in augmentation in heat transfer rate to 600%. The natural convective flow mechanism and heat exchange under a magnetic field within a concentric circular annulus between a heat-generating conductive internal cylinder and an isothermally cold external cylinder filled with a CNTswater-based nanoliquid is investigated by Tayebi, Oztop et al. (2021).

Al-Azzawi et al. (2021) examined heat transfer performance in a brass body of a concentric vertical cylinder and the effect of induced vibration on the system. The results indicated that the heat transfer rate was improved and increased, and the thermal boundary layer increased from the bottom to the top surface under vibration. In addition, the Rayleigh number had a negative effect on the heat transfer rate, whereas the vibration Reynolds number positively impacted the heat transfer rate during the vibration. Tayebi and Chamkha (2021) investigated the influences of local thermal non-equilibrium on thermo-natural convection in an elliptical annular space separated by a nanofluid-saturated porous sleeve using the standard SIMPLER algorithm. Tayebi, Chamkha, et al. (2021) explained the effect of a solid conductive partition on the thermal-free convective motion mechanism and heat

transmission process within a concentric circular annulus filled with a water-based hybrid nano liquid containing copper and alumina nanoparticles.

Tayebi et al. (2022) conducted a comprehensive and accurate numerical analysis of the local thermal non-equilibrium effects on the natural convection characteristics in a horizontal elliptical porous annulus saturated with nanofluid using a finite volume technique. In the presence of magnetic fields, Tayebi et al. (2022) performed a numerical analysis of thermo-natural convection and entropy generation in an alumina-water nanofluid enclosed by two circular cylinders.

According to the literature, many experimental and theoretical studies have investigated the influence of vibration on convective heat transfer. Different structures such as flat plates, cylinders, wires, and various shapes of enclosed cavities; for different orientations have been used. The vibration vector was analyzed relative to these surfaces; for other vibration parameters, including amplitude and frequency, based on various heating conditions.

The motivation of this investigation purpose is to scrutinize the influence of vibration frequency, Rayleigh number ($Ra = 10^2, 10^3, 10^4, 10^5, \text{ and } 10^6$), eccentricity, and vibration Rayleigh number ($Rav = 10^2, 10^3, 10^4, \text{ and } 10^5$) on the natural heat transfer rate performance using a horizontal annulus with a vibrating inner cylinder. The emphasis is on the inner vibration cylinder being heated under constant heat flux subjected to vertical sinusoidal vibrations and eccentricity on the temperature and flow fields. The range of vibration frequency ($\omega = 0, 100, 1000 \text{ \& } 10000$) and the Prandtl number is 0.7. According to changes in vibration frequency from low to high, flows and heat transfer rates were altered from a quasi-static state zone via a resonant region. Furthermore, we also examine the results of two vertical eccentricities of the streamlines, isothermal lines, and the changes in the fluid's Nusselt number and those for concentric arrangement. Meanwhile, the mechanical vertical vibration effects have been successfully used to control heat and mass transfer, such as in heat exchangers, stirrers, mineral separators, nuclear reactors, and crystal growth. Therefore, a good understanding of the fundamental theory of thermal vibrational convection behind those applications and phenomena is necessary. So, this is the motivation, the "innovation", and the main contribution of this paper.

In addition to the results for the concentric configuration, results for two vertical eccentricities of the streamlines, isothermal lines, and variations in the fluid's Nusselt number are presented. The following is the structure of this paper; the mathematical statement of the problem is supplied in the next section. Then there are the governing equations and the numerical approach. Next, changing the cylinder's Rayleigh number, eccentricity, and vibration frequency on the streamlines, isotherms, and temporal average Nusselt number will be illustrated and discussed. Finally, some closing remarks are included.

MATERIALS AND METHOD

A sketch of the physical model for consideration is shown in Figure 1. The annulus is formed by two cylinders: vertically eccentric and horizontally centric. The outer cylinder, with a radius (R_o), is fixed in this model. However, the inner cylinder, with a radius (R_i), may be adjusted vertically to vary the eccentricity and can be vertically vibrated with frequency (Ω). A positive eccentricity (ϵ) between two cylinders is achieved if the inner cylinder's center is higher than the outer cylinder's. In contrast, a negative eccentricity (ϵ) would be achieved if the inner cylinder was oriented vertically in five different ways.

The annulus contains air (as working fluid $Pr = 0.7$), and the inner wall of the annulus is heated at constant heat flux (q_i), while the annulus's outer wall is cooled and kept at a constant temperature (T_o). Initially ($t = 0$), the inner cylinder is at the center of the annulus, the air in the annulus is stationary, and its temperature and the cylinder's surface are kept at $T_s = T_o$. Afterward ($t > 0$), the inner cylinder is forced to vertical vibration with displacement ($-b \sin \Omega t$) parallel to the gravity vector, the inner cylinder's buoyancy and vibration impact heat transfer from the inner cylinder to the outer cylinder.

The following assumptions are made:

1. The fluid is Newtonian (air), and the flow is 2-D space formed between two eccentric horizontal cylinders to make the analysis more accessible.
2. The vibration amplitude ($b\Omega$) is small, and the flow is incompressible and laminar.
3. The Boussinesq assumption is correct; viscous dissipation, heat generation, and the radiation heat transfer impact are disregarded.
4. The characteristics of air are assumed constant, and the density of the fluid is considered constant except for density in buoyancy terms.
5. There is no-slip condition held on the interfaces between the fluid and surface.
6. The induced vibration is in the vertical direction and parallels gravity.
7. The eccentricity, ϵ the two cylinders, is taken positively if the center of the inner cylinder is above the outer cylinder and negative if below it.

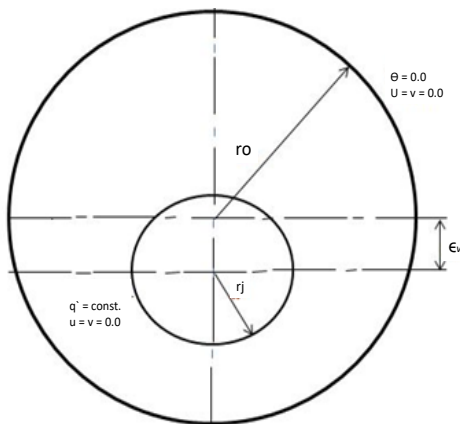


Figure 1. Geometry of annulus

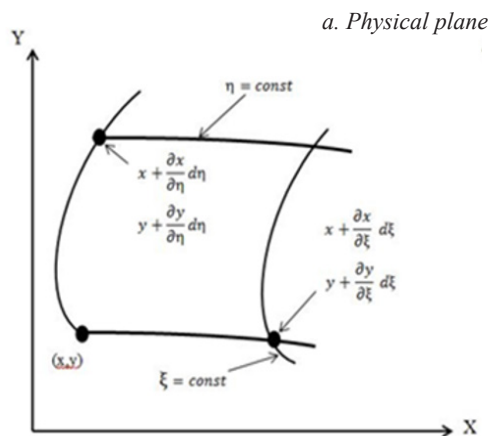


Figure 2. Physical and transformed computational planes

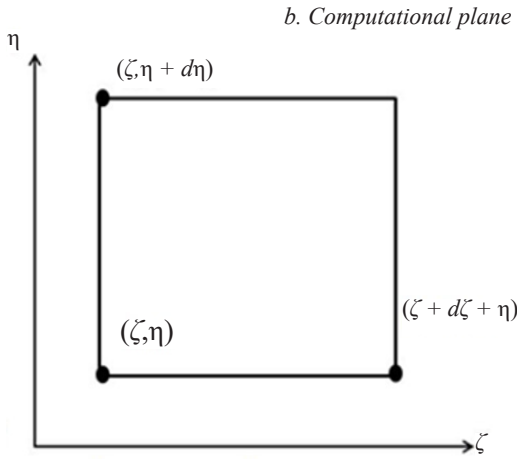


Figure 2. (Continue)

Mathematical Formulation [Coordinate Transformation & Governing Equations] Method

Thompson et al. (1974) proposed a numerical mapping method to generate a body-fitted coordinate system (BFCs) to overcome the problems associated with the complex physical domain. This method enables us to approximate or interpolate at the outside limits of the body. Navier-Stokes equations in the dimensionless form are governing equations for the conservation of mass, momentum, and energy. The energy equation in Cartesian coordinates is written in Table 1, the in-stream function - vorticity formulation.

Table 1

Navier-Stokes equations in dimensionless form, and the energy equation in Cartesian coordinates

$X, Y = \frac{x, y}{L}, L = \frac{D_o - D_i}{2} = R_o - R_i$	$\theta = \frac{(T - T_c)K}{q''L}$
$u_{ref} = \frac{\alpha}{L}$	$\omega = \frac{\Omega}{\Omega_r} = \frac{\Omega L}{u_{ref}}; \Omega_r = \frac{u_{ref}}{L}$
$\tau = \frac{t}{t_r} = \frac{t u_{ref}}{L}; t_r = \frac{L}{u_{ref}}$	$\Psi = \frac{\varphi}{\varphi_r}, \varphi_r = u_{ref}L$
$\rho^* = \frac{\rho}{\rho_{ref}}, \mu^* = \frac{\mu}{\mu_{ref}}$	$W = \frac{\omega}{\omega_r}, \omega_r = \frac{u_{ref}}{L}$
$Pr = \frac{\nu}{\alpha} = \frac{\mu C_p}{K}$	$Ra = \frac{\rho^2 g_o \beta q'' L^4}{K \mu^2} Pr$
$Gr_{vib} = \frac{1}{2} \left[\frac{\rho^2 (b\Omega) \beta q'' L^2}{K \mu^2} \right]^2$	$Ra_{vib} = \frac{1}{2} \left[\frac{\rho^2 (b\Omega) \beta q'' L^2}{K \mu^2} \right]^2 Pr$

The horizontal and vertical components of velocity can be re-written in the transformed plane as given in Equations 1 and 2:

$$U = \frac{1}{J}(\Psi_\eta \cdot X_\xi - \Psi_\xi \cdot X_\eta) \tag{1}$$

$$V = \frac{1}{J}(\Psi_\eta \cdot Y_\xi - \Psi_\xi \cdot Y_\eta) \tag{2}$$

The stream function-vorticity formulation in an elliptic partial differential equation can be hung to the following generic form in computational space (ξ, η) . A generalized scalar's Laplacian in the converted plane may be given as Equations 3 and 4:

$$\frac{1}{J^2}(\lambda \cdot \Psi_\xi + \sigma \cdot \Psi_\eta + \alpha \cdot \Psi_{\xi\xi} - 2\beta \cdot \Psi_{\xi\eta} + \gamma \cdot \Psi_{\eta\eta}) = -W \tag{3}$$

$$W_\tau + \frac{1}{J}(-\Psi_\xi \cdot W_\eta + \Psi_\eta \cdot W_\xi) = \frac{Pr}{J^2}(\lambda \cdot W_\xi + \sigma \cdot W_\eta + \alpha \cdot W_{\xi\xi} - 2\beta \cdot W_{\xi\eta} + \gamma \cdot W_{\eta\eta}) + \frac{1}{J}[(y_\eta \frac{\partial \theta}{\partial \xi} - y_\xi \frac{\partial \theta}{\partial \eta})][PrRa + \varpi \sqrt{PrRa_{vib}} \sin \varpi \tau] \tag{4}$$

And by substituting the parameters of the transformed computational field (ξ, η) in the equation of energy, it becomes Equation 5:

$$\frac{\partial \theta}{\partial \tau} + \frac{1}{J}(-\Psi_\xi \cdot \theta_\eta + \Psi_\eta \cdot \theta_\xi) = \frac{1}{J^2}(\lambda \cdot \theta_\xi + \sigma \cdot \theta_\eta + \alpha \cdot \theta_{\xi\xi} - 2\beta \cdot \theta_{\xi\eta} + \gamma \cdot \theta_{\eta\eta}) \tag{5}$$

Hence, introducing the following parameters, where (J) is the (Jacobian of the transformation) defined as Equations 6 to 10:

$$J = x_\xi y_\eta - x_\eta y_\xi \tag{6}$$

$$\left\{ \begin{array}{l} \alpha = x_\eta^2 + y_\eta^2 \\ \beta = x_\xi x_\eta + y_\xi y_\eta \\ \gamma = x_\xi^2 + y_\xi^2 \end{array} \right\} \tag{7}$$

$$\left\{ \begin{array}{l} D_x = \alpha \cdot y_{\xi\xi} - 2\beta \cdot y_{\xi\eta} + \gamma \cdot y_{\eta\eta} \\ D_y = \alpha \cdot x_{\xi\xi} - 2\beta \cdot x_{\xi\eta} + \gamma \cdot x_{\eta\eta} \end{array} \right\} \tag{8}$$

$$\lambda = \frac{1}{J}(x_\eta \cdot D_y - y_\eta \cdot D_x) \tag{9}$$

$$\sigma = \frac{1}{J}(y_\xi \cdot D_x - x_\xi \cdot D_y) \tag{10}$$

The non-dimensional initial and BCs can be represented in Equations 11 to 15:

$$\text{at } \tau = 0 \quad w = \psi = U = V = \theta = 0$$

1. At the inner cylinder ($\eta = \eta_i$), $\Psi(\xi_i, \eta) = U = V = 0$

$$W^{k+1}(i, w) = \frac{-3\gamma_{(i,w)} \cdot (\Psi_{(i,w+1)} - \Psi_{(i,w)})}{\Delta\eta^2 \cdot J^2_{(i,w)}} - \frac{W_{(i,w+1)}}{2.0} \quad [11]$$

$$\xi_x \frac{\partial \theta}{\partial \xi} + \eta_x \frac{\partial \theta}{\partial \eta} = \frac{1}{J} \left(y_\eta \frac{\partial \theta}{\partial \xi} - y_\xi \frac{\partial \theta}{\partial \eta} \right) = -1 \quad [12]$$

The above equation can be re-written as

$$\theta(i, j) = \theta(i, j + 1) - \frac{\beta(i,j)}{2\gamma(i,j)} \cdot [\theta(i + 1, j) - \theta(i - 1, j)] + J\sqrt{\gamma} \cdot \frac{\Delta\eta}{\gamma} \quad [13]$$

2. At the outer cylinder ($\eta = \eta_o$), $\Psi(\xi_o, \eta) = U = V = 0$

$$W^{k+1}(i, w) = \frac{-3\gamma_{(i,w)} \cdot (\Psi_{(i,w-1)} - \Psi_{(i,w)})}{\Delta\eta^2 \cdot J^2_{(i,w)}} - \frac{W_{(i,w-1)}}{2.0} \quad [14]$$

$$\theta(i, j - 1) = 0 \quad [15]$$

The stream function is zero because the cylinder is a continuously solid surface, entering or exiting it. The non-dimensional heat transfer coefficient of local Nusselt number Nu can be found in Equations 16 and 17:

$$Nu = - \left(\frac{\partial T}{\partial r} \right)_{y=y_i} * \frac{L}{(T_H - T_c)} \quad [16]$$

$$Nu = \frac{1}{\theta} \quad [17]$$

The average Nusselt number may be calculated by integrating the local Nusselt number, which yields the below Equation 18:

$$\overline{Nu} = \frac{\bar{h} L}{k} \quad [18]$$

Method of Solution and Numerical Technique

Grid Generation. The numerical method employed in the current study is discussed in this section, grid generation; because of the complexity of the physical shape used, we use the body-fitted coordinate system (BFC) technique first proposed by Thomson et al. (1974). After that, a curvilinear grid was created by solving two elliptic differential equations. Then, it was used to solve vorticity-stream equations in the vicinity of complex bodies (Figure 2) without the need to use approximating or interpolating at the outside limits of the body given as Equations 19 and 20:

$$\xi_{xx} + \xi_{yy} = P(\xi, \eta) \tag{19}$$

$$\eta_{xx} + \eta_{yy} = Q(\xi, \eta) \tag{20}$$

P and Q are coordinate control functions that can focus the coordinate lines on domain areas with high fluctuations of a given characteristic. The physical coordinates can be used as the dependent variable in Equations 21 and 22:

$$\alpha x_{\xi\xi} - 2\beta x_{\xi\eta} + \gamma x_{\eta\eta} + J^2(Px_{\xi} + Qx_{\eta}) = 0 \tag{21}$$

$$\alpha y_{\xi\xi} - 2\beta y_{\xi\eta} + \gamma y_{\eta\eta} + J^2(Py_{\xi} + Qy_{\eta}) = 0 \tag{22}$$

The transformation coefficients and Jacobian are defined in Equations 6, 7, 9, and 10.

Discretization Technique and Method of Solution. The numerical solution for the governing equations used general curvilinear coordinates ($x = x(\xi, \eta)$, $y = y(\xi, \eta)$) are solved in the stream function-vorticity formulation (Ψ, \mathbb{W}) to avoid enforcing the additional integral demand for the single pressure interpretation. The mesh of the generated model available in the form of the bipolar coordinate system was illustrated in Figure 3, where the (radial-like curves) represent constant angles in angular coordinate (ξ), and the eccentric circles indicate constant lines (η). The eccentricity and azimuthal position of the inner circle were easily obtained by changing the location of the inner cylinder and vibrating it in a direction parallel to gravity acceleration. Equations 3 to 5 are solved by successive line over-relaxation LSOR technique. The partial differential equations use second-order central-difference schemes for all derivatives. Figure 3 depicts the computation mesh with the internal cylindrical part in 5 different vertical locations within the outer cylindrical surface (centric) and for the vertical eccentric annulus configuration ($\epsilon = -0.625, -0.333, 0, +0.333 \text{ \& } +0.625$).

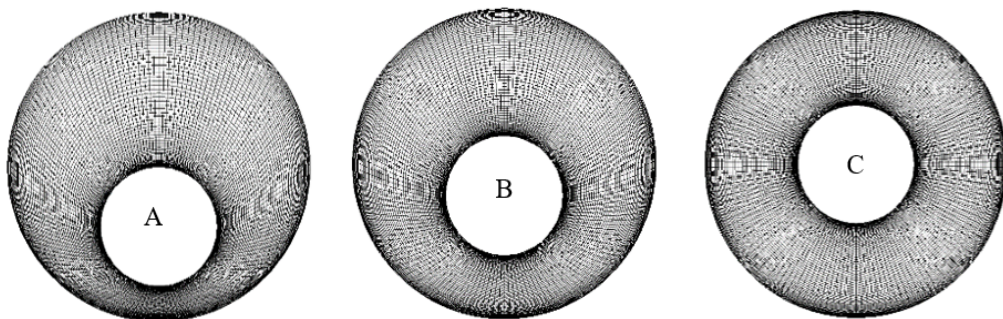


Figure 3. Inner cylinder location and computational mesh for A: $\epsilon = -0.625$; B: $\epsilon = -0.333$; C: $\epsilon = 0$

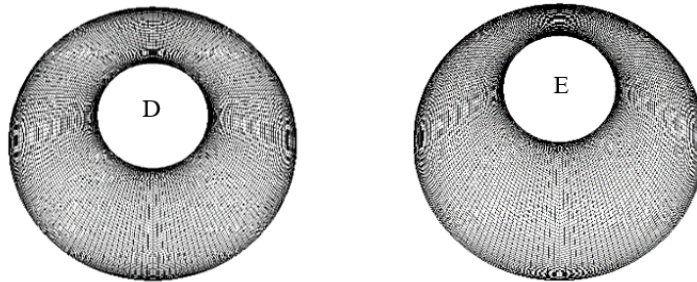


Figure 3 (Continue). Inner cylinder location and computational mesh for D: $\epsilon = +0.333$; E: $\epsilon = +0.625$

Since the domain's boundaries do not lie along natural coordinates, a boundary-fitted nonorthogonal coordinate system is used. The solution procedure involves grid generation, discretization of the governing equations, and an algorithm for solving the equations. The finite difference method in the transformed plane solves the design of governing Equations 3 to 5. In the second-order central difference scheme, except for the convective terms in the two transport equations which utilize the standard major plan, all the spatial discretization is done with them. The stability of the numerical method is investigated for case $= 10^6$ and all frequencies. The time steps are chosen with values of 0.00001. A nonuniform grid field has been used for the radial direction, which has smoothly varying grid spacing with a denser grid near the inner and outer walls of the annulus to account for the boundary layers formed in these regions. The mesh size 175×76 is used for a grid independence study of numerical results for all cases. It is noted that the total number of grid points is 100000. Dirichlet conditions are stated at the boundaries.

NUMERICAL VALIDATION

In this study, the flow field is based on streamlines, and the thermal area uses isotherms for the following parameters ($Ra = 10^3, 10^4, \text{ and } 10^5$), ($\epsilon = \pm 0.625$), radii ratio ($\frac{r_o}{r_i} = 2.6$), and keeping the ratio of gap width to diameter ($\frac{L}{Di} = 0.8$) for a fluid with ($Pr = 0.7$). Figures 4 and 5 show comparisons (in the absence of vibration and constant temperature boundary conditions) between the flow pattern of the streamlines and isotherms of numerical results, which contain 0.5 of the isotherms and 0.5 of the respective streamlines. Figures 4 and 5 show reasonable matching with eccentric inner cylinder configurations beyond a simple qualitative interpretation.

Kuehn and Goldsten (1976) conducted extensive computational and experimental research on concentric annuli; a test run was carried out for ($Ra = 5 \times 10^4$). Figure 6 explains the results of the Local equivalent thermal conductivity (k_{eq}). A strong consensus can be seen with the tests and validated by Kuehn and Goldstein (1976; 1978) for outer and inner cylinders. Furthermore, the maximum surface temperature (MST) results on the inner

cylinder and the average Nusselt number are compared with the data found by Ho et al. (1989) using the same characteristics and without vibration. Another practical parameter is the size of the MST on the inner surface of the homogeneous Heat flow, shown in Tables 2 and 3, which appears to be consistent with those predicted in the current study.

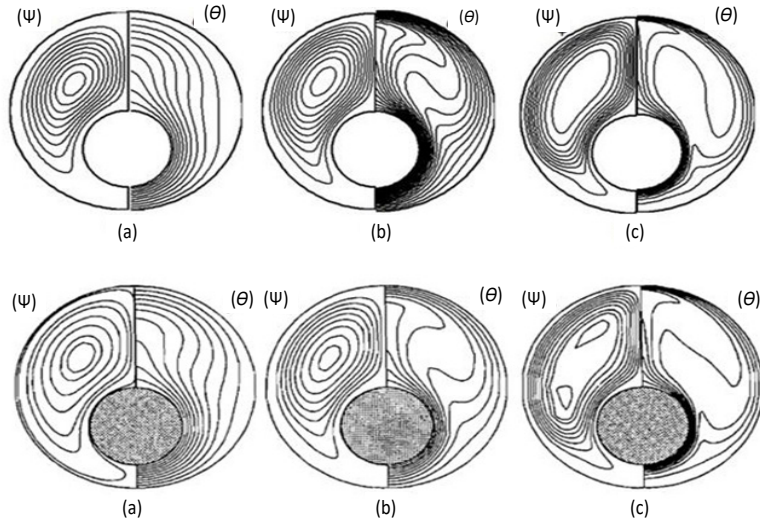


Figure 4. Comparison streamlines (left half), and isotherms (right half), $Pr = 0.7$; $\epsilon = -0.625$; $(\frac{L}{D_i}) = 0.8$: upper, present. method; lower, from (Projahn et al., 1981). (a) $Ra = 10^3$; (b) $Ra = 10^4$; (c) $Ra = 10^5$

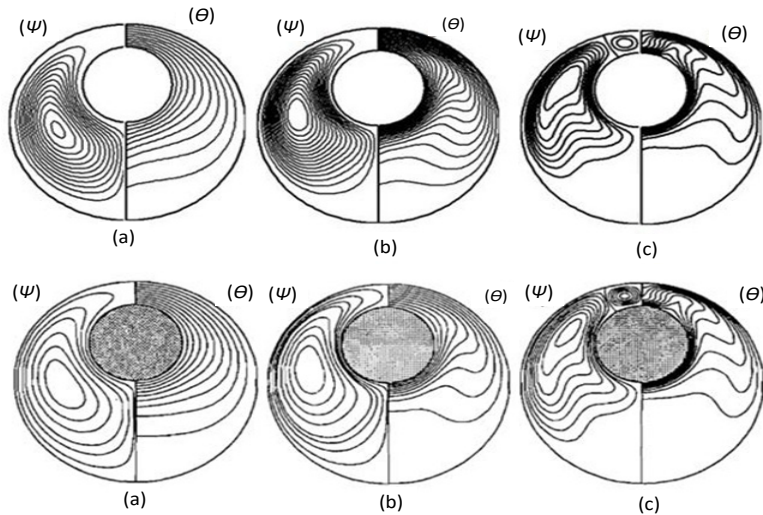


Figure 5. Comparison streamlines (left half), and isotherms (right half) $Pr = 0.7$, $\epsilon = +0.625$; $(\frac{L}{D_i}) = 0.8$: upper, present method; lower, from (Projahn et al., 1981). (a) $Ra = 10^3$; (b) $Ra = 10^4$, (c) $Ra = 10^5$

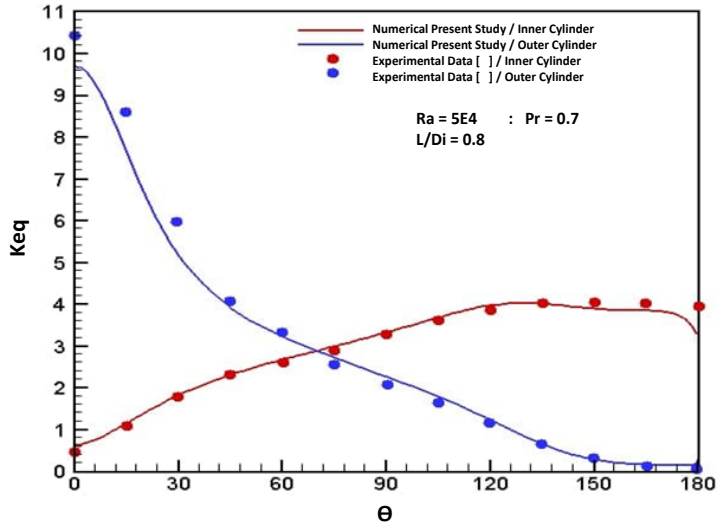


Figure 6. Validation of Concentric local heat transfer coefficients at $Ra = 10^5, Pr = 0.7, \epsilon = 0, \left(\frac{L}{Di}\right) = 0.8$, from (Kuehn & Goldstein, 1976).

Table 2

MST on the inner cylinder of the uniform heat flux at Ra

ϵ	Pr	10^3	10^4	10^5	10^6
0.625 (present study)	0.700	0.550	0.451	0.400	0.201
+ 0.625 (Ho et al., 1989)	0.700	0.562	0.468	0.445	0.358
0 (present study)	0.700	0.651	0.530	0.36	0.240
0 (Ho et al., 1989)	0.700	0.696	0.525	0.347	0.229
- 0.625 (present study)	0.700	0.641	0.432	0.33	0.221
- 0.625 (Ho et al., 1989)	0.700	0.648	0.444	0.331	0.227

Table 3

Average Nusselt number

ϵ	Pr	10^3	10^4	10^5	10^6
0.625 (present study)	0.700	2.137	2.515	3.785	6.622
+ 0.625 (Ho et al., 1989)	0.700	2.272	3.207	4.482	6.894
0 (present study)	0.700	1.705	2.667	4.310	6.588
0 (Ho et al., 1989)	0.700	1.731	2.763	4.418	6.729
- 0.625 (present study)	0.700	2.394	3.096	4.371	6.806
- 0.625 (Ho et al., 1989)	0.700	2.048	2.610	3.911	6.390

RESULTS AND DISCUSSION

As previously stated, the primary goal of this research is to evaluate fluid flow and heat transfer characteristics at vibrating concentric and eccentric horizontal cylinders. Therefore, all numerical computations were completed for the Rayleigh number ($10^2 \leq Ra \leq 10^6$) based on the radius difference (L : is the mean gap width = $R_o - R_i$), vibrational Rayleigh number $0 \leq Ra_{vib} \leq 10^5$, non-dimensional vibrational frequencies ($\omega = 0, 100, 1000 \text{ \& } 10000$), and besides the influence of vibration, eccentricity reveals themselves as local flow and temperature field disturbances. For example, the concentric case with four eccentricities yielded results ($\epsilon = 0, \pm 0.625 \text{ \& } \pm 0.333$), radii ratio ($\frac{R_o}{R_i} = 2.6$) while preserving the gap width/diameter ratio ($\frac{L}{D_i} = 0.8$) for a fluid with ($Pr = 0.7$).

Flow and Temperature Fields

This section presents fluid and heat transfer properties represented by the streamlines and isotherms. The streamlines and temperature contoured when the inner was changed vertically within the outer cylinder for different Rayleigh numbers and various frequencies shedding on the inner cylinder.

Eccentricity's Influence (Effect of Inner Cylinder Position)

A computation with precise parameters of ($Ra = 10^4$, $Ra_v = 10^5$, $\omega = 1000$) and contour plots of stream functions and isotherms are shown to visualize the flow evolution in Figures 7a and 7b. When the heated inner cylinder is in the concentric position $\epsilon = 0$, Figure 7a (C), the streamlines and isotherms show that the hot flow tends to move upward due to thermal expansion along the vertical symmetry line. As the air impinges the cold wall of the outer cylinder, it becomes colder and denser; thus, it moves radially away from the cold wall and downward again. Thus, two similar recirculation air pockets are formed on the side of the vertical symmetry line with the center of the cylinders. The effect of the heated inner cylinder moving vertically upward to the center of the outer cylinder $\epsilon = (+0.625 \text{ and } +0.333)$ Figures 7a (D & E) presses air at the top, and vacant space is induced at the bottom. These two actions force air at the top region to flow to the bottom region. The forced convection due to the inner cylinder vibration affects the natural convection flow and thermal transport in the annulus. The astonishing vortex splitting as the vortex core is halved and bisected (closest position to the upper wall of the inner cylinder), the flow tends to separate by approaching cylinders at $\epsilon = +0.625$ is depicted consecutively in Figure 7a (E). As the heated inner cylinder is moved vertically down to the center of the outer cylinder, the flow does not separate, and a center with large plumes occurs. Hence the pump is hot air toward the upper wall along the vertical symmetry line, as shown for the negative eccentric position ($\epsilon = -0.625 \text{ and } -0.333$). Figure 7a (A & B) illustrate that the

inner cylinder is located at the bottom region, the air at the bottom is pressed, and vacant space is induced at the top region, reversing the flow direction.

Figure 7(b) shows the isotherms in the annulus during the vibration for different inner cylinder positions at the same vibrational frequency $\omega = 1000$. The inner cylinder in the concentric position $\epsilon = 0$ in Figure 7b (c) indicates a wide temperature zone at the top region. It is due to the buoyancy effect promoted by the changes in the mass density, and the reverse is noted in the bottom region. As the inner cylinder is on its way to moving upward $\epsilon = (+0.625$ and $+0.333)$ Figures 7b (D & E), the heat transfer between the inner and outer cylinder is affected by the movement of the inner cylinder. The isothermal lines are dense at the top region, showing high heat flow in this region. At the bottom region, the heat flow is dominated by conduction, making the heat transfer rate low. When the inner cylinder moves upward $\epsilon = +0.625$, the conduction region expands, reducing heat flow. At this instant, the heat transfer in the annulus is less than that of the concentric annulus case. At the negative eccentricity ($\epsilon = -0.333$) and -0.625 Figures 7b (A & B), the heat transfer rate at the bottom region is extensively promoted by reducing the thermal boundary layer (thermal resistance). Also, the convection cell at the top region is expanded by strong convection, enhancing the heat flow in this region. When the eccentricity of the inner cylinder is minimal, the heat transfer from the inner cylinder to the outer cylinder reaches its maximum value.

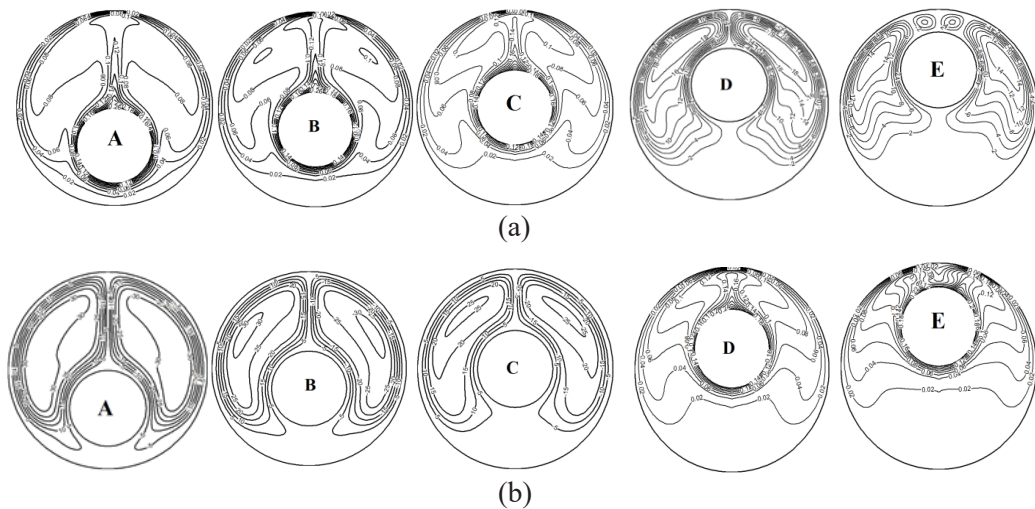


Figure 7. (a). Streamlines, (b). Isotherms; at $RaL = 10^4$, $Ra_v = 10^5$, vibrational frequency $\omega = 1000$, at different eccentricity (A) $\epsilon = -0.625$, (B) -0.333 , (c) 0 , (D) $+0.333$, (E) $+0.625$, respectively.

The Effect of Rayleigh's Number Ra_L . The effect of the Rayleigh number on the kinematic and thermal fields (streamlines and isotherms) are shown in Figures 8 and 9 for ($10^2 \leq Ra \leq 10^6$), $Ra_{vib} = 10^5$, $\varpi = 1000$, and $\epsilon = (-0.625$ and $+0.625)$ from these results, and it can be seen that the flow is symmetrical concerning the medium vertical axis passing through the center of these cylinders. For each case, the flow over the inner cylinder creates a circulation zone on both sides of the cavity for all values of the Rayleigh number. The flow is organized in two main counter-rotating cells. The flow is organized into two central contour-rotating cells. The cell on the left rotates counterclockwise while the suitable cell rotates clockwise. It is due to the strength of buoyancy produced by the temperature gradient. According to these conditions, the fluid is raised on the side of the inner cylinder, leading to flow becoming fresh and denser in the outer cylinder. At ($\epsilon = +0.625$), show that at low $Ra = 10^2, 10^3, 10^4$. The remarkable process of outer vortex splitting by increasing the Rayleigh number is sequentially observed in Figures 8a and b (A, B & C). As a result, the laminar convection is weak, and the values of the current function are shallow and almost similar. In these cases, the heat transfer is mainly by conduction. By increasing the Rayleigh number to $Ra = 10^5$ and then to 10^6 , with ($\epsilon = +0.625$), we are in a pseudo-conductive regime. The thermal transfers are, therefore, essentially conducive. The values of the current function appearing in Figures 8 and 9 are always small so that the conduction dominating flow region at the narrowest gap of the annuli becomes locally stagnant, continuously splitting the outer vortex core in the constricted region into two sub vortices rotating in the same direction. In the broader part of the eccentric annulus, the vortex current is slowed down, and the location of its core is upper at $Ra = 10^6$, as shown in Figures 8a and 8b (D & E). The convection eddy is relatively vigor and produces a clockwise symmetrical recirculation, unlike positive eccentricity ($\epsilon = +0.625$), so the impact of the secondary flow cell at the top is reflected in the form of the isotherm. Increasing Rayleigh to 10^5 means a higher stream function absolute value causes an intensified internal convection eddy and a more excellent fluid motion; as the Rayleigh further increases to $Ra = 10^6$, the inner vortex grows and becomes more extensive than at $Ra = 10^5$, as shown in Figures 9a (D & E).

The effect of Rayleigh number as the inner cylinder at the bottom region $\epsilon = -0.625$ the reverse demeanor is noticed in the bottom region as shown in Figures 9a and 9b. In the inner cylinder, the global flow joins near the bottom of the inner wall and connects with the inner wall's top, while secondary vortices over the top disappear and diminish. When the inner cylinder moves downward, more spaces between the hot inner cylinder and the top cold wall are secured, enhancing the buoyancy-induced convection. Thus, isotherms move upward, and more enormous plumes exist on the top of the inner cylinder, which increases the thermal gradient on the top of the annulus. As the form of the dominant flow at the upper half of the annulus, the recirculating eddies form there, so Rayleigh increases to 10^5 , and the stagnant region under the heated inner cylinder decreases.

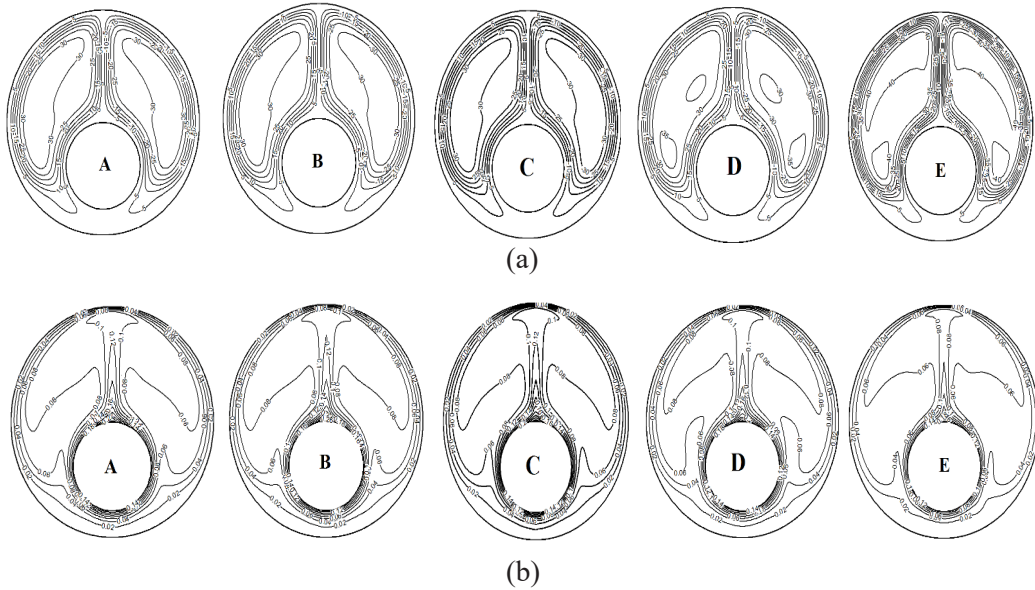


Figure 8. (a) Streamlines and (b) Isotherms of annuli of the eccentricity $\epsilon = -0.625$ and $\epsilon = +0.625$, respectively; vibrational frequency $\omega = 1000$, $Ra_{vib} = 10^5$, $\frac{L}{Di} = 0.8$ at different $Ra = (A)10^2$, (B) 10^3 , (C) 10^4 , (D) 10^5 , (E) 10^6 .

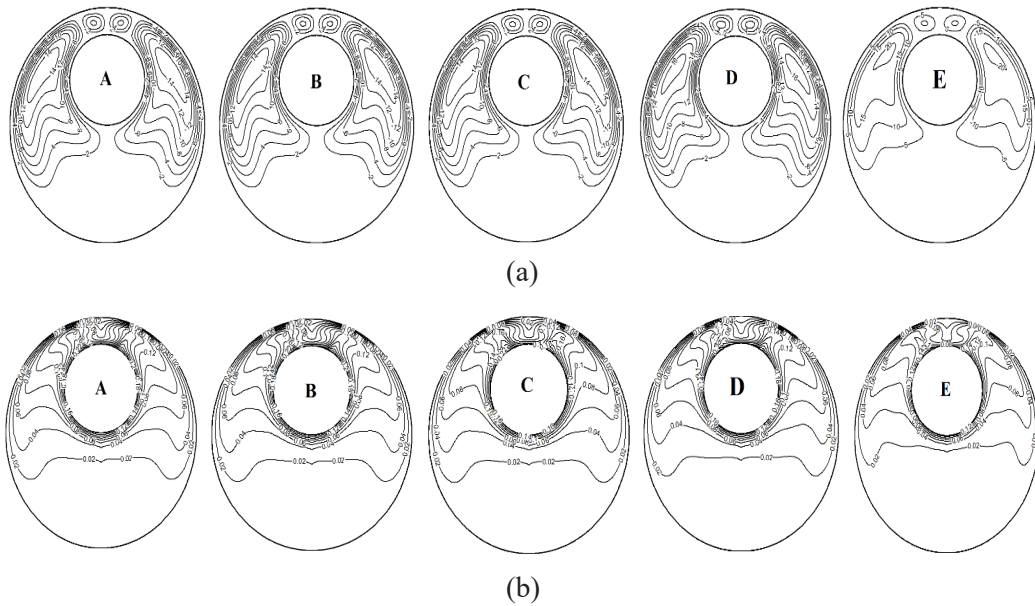


Figure 9. (a) Streamlines and (b) Isotherms of annuli of the eccentricity $\epsilon = +0.625$; vibrational frequency, $Ra_{vib} = 105$, $\omega = 1000$, at different $Ra = (A)10^2$, (B) 10^3 , (C) 10^4 , (D) 10^5 , (E) 10^6

Vibration Frequency's Influence

Figures 10 and 11 comparatively present the influence of vibrational frequency on the variations of streamlines and isotherms at $Ra = 10^4$, $Ra_{vib} = 10^5$, $\epsilon = (-0.625, \text{ and } +0.625)$. The vibration frequency changed ($\varpi = 0, 100, 1000 \text{ and } 10000$). Initially, the system is at a static case ($\varpi = 0$) without vibration. It is used for analysis and comparisons. In Figures 10a and 11a (B), the inner cylinder commences vibrating vertically, even at a low frequency ($\varpi = 100$). The influence of dynamic response on the fluid flow is extraordinary, as the thermal vibrational convection is weak at a moderate value $Ra = 10^4$. As the frequency increases to ($\varpi = 1000$) near the resonant frequency, it can be inferred that the fluid movement is becoming more apparent, and the variations in the streamlines and isotherms are quite different from those of static convection and previous circumstances.

Two outer counter-rotating eddies are formed at the vertical position $\epsilon = +0.625$, strongly influencing the heat transfer. The vibration effect is more remarkable than when the vibrational frequency rises ($\varpi = 10000$). During the vibration of the inner cylinder, as it shifts upward and the fluid near the upper region of the cylinder will be pressed by the cylinder surfaces; on the other hand, the fluid near the lower region of the cylinder simultaneously replenishes the vacant space induced by the cylinder's movement due to the continuity law. A similar phenomenon occurs when the direction of movement of the inner cylinder changes, resulting in refilled empty spaces near the upper regions. As a result of internal cylinder vibration at the vertical position $\epsilon = +0.625$, a tiny vortex appears at the top part of the cylinder. Due to isotherms distortion caused by vibration, some portion of the hot flow will be located inside the hot flow, discovered inside the cold fluid region, and lose their high temperature. As a result, the colder and, thus, denser fluids will descend. The colder fluids meet hot liquid again during their descent due to isotherms' distortion and will be heated again and cause an eddy appearance. As the cylinder oscillates, isotherms become distorted, and new vortices will come into sight. Cylinders' upward and downward movements give vortices appropriate to growth and ascent.

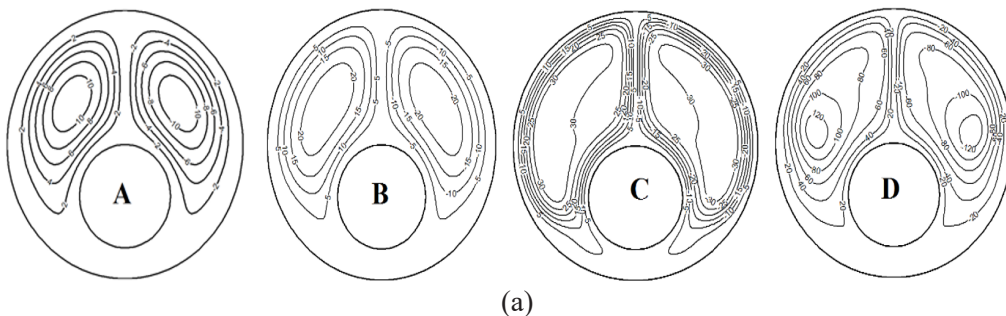


Figure 10. (a) Streamlines and (b) Isotherms of annuli of the eccentricity $\epsilon = -0.625$; $Ra = 10^4$, $Ra_{vib} = 10^5$, $r_o/r_i = 2.6$, and $\frac{L}{Di} = 0.8$ but in different vibrational frequency

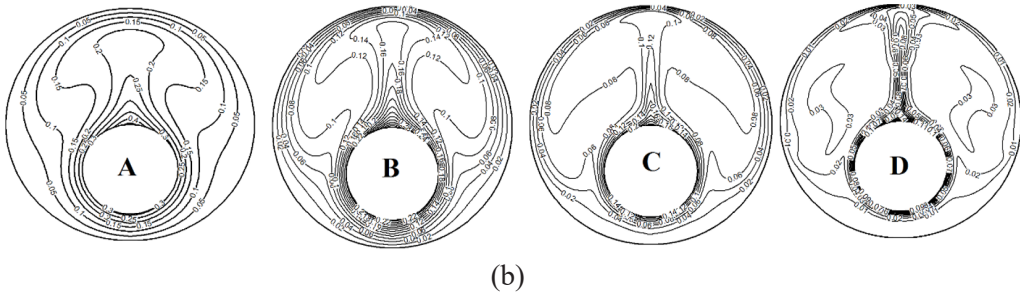


Figure 10. (Continue)

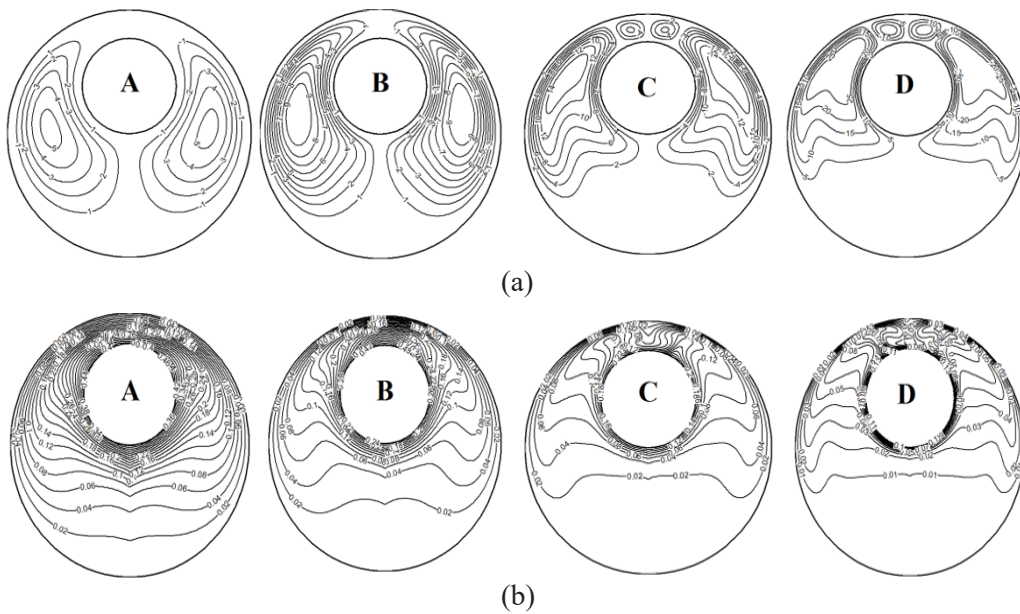


Figure 11. (a) Streamlines and (b) Isotherms of annuli of the eccentricity $\epsilon = +0.625$; $Ra = 10^4$, $Ra_{vib} = 10^5$, $(ro/ri) = 2.6$, $\frac{L}{Di} = 0.8$ but in different vibrational frequency (A) $\omega = 0$, (B) $\omega = 100$, (C) $\omega = 1000$, and (D) $\omega = 10000$.

Local Nusselt Number (Nu)

Effect of Eccentricity (Effect of Inner Cylinder Position). Figures 12a, 12b, and 12c show the distribution of the local Nusselt number at various angles along the circumference of the inner cylinders at $Ra = 10^4$, $0 \leq Ra_{vib} \leq 10^5$, ($\omega = 1000$) and for different vertical inner cylinder locations with concentric an eccentric $\epsilon = (-0.625, -0.333, 0, +0.333$ and $+0.625$). Because the stream and temperature patterns are found for cases $\epsilon = -0.333$ almost similar at $\epsilon = -0.625$ and $\epsilon = +0.333$ similar to the case at $\epsilon = +0.625$, the results at $\epsilon = -0.333$ and $\epsilon = +0.333$ are not presented here for the sake of brevity. However, if there is any difference between those, it will be mentioned. The results for concentric $\epsilon = 0$ and negative eccentric

$\epsilon = -0.625$ geometry are qualitatively similar and will be discussed. The minimum Nu is seen at the top of the cylinder ($\phi = 180^\circ$), where the plume occurs and the isotherm contour coarsest. The maximum Nu is shown to be at ($\phi = 0^\circ$), where the temperature contours are densest due to the movement of the upward-directed cold fluid. (Nu) increases from the bottom of the ($\phi = 0^\circ$) to the top ($\phi = 180^\circ$) of the inner cylinder.

As Ra_{vib} increases, the angular variation of (Nu) becomes more pronounced such that the heat transport is highly concentrated in the upper half of the inner cylinder. The effect of positive eccentricity $\epsilon = +0.625$ on Nu is quite different from the two cases described before, as depicted in Figure 12c. At the region from ($\phi = 0^\circ$ to 120°), (Nu) behaved as two cases for the behavior $\epsilon = 0$, and -0.625 as mentioned above. At ($\phi = 120^\circ$), the deflection of the Nusselt number is seen. This peculiar behavior is due to the existence of the secondary flow cell above the inner cylinder, which develops for $Ra_{vib} > 10^4$ convection and has a minor influence at the bottom of the annulus $\phi = 0^\circ$, where the boundary layer starts to develop and is still thin. On the contrary, at ($\phi > 150^\circ$), the minimum heat transfer rate shifts to the maximum, increasing the vibrational Rayleigh number. The maximum due to convection becomes pronounced when the vibrational Rayleigh number exceeds 10^4 .

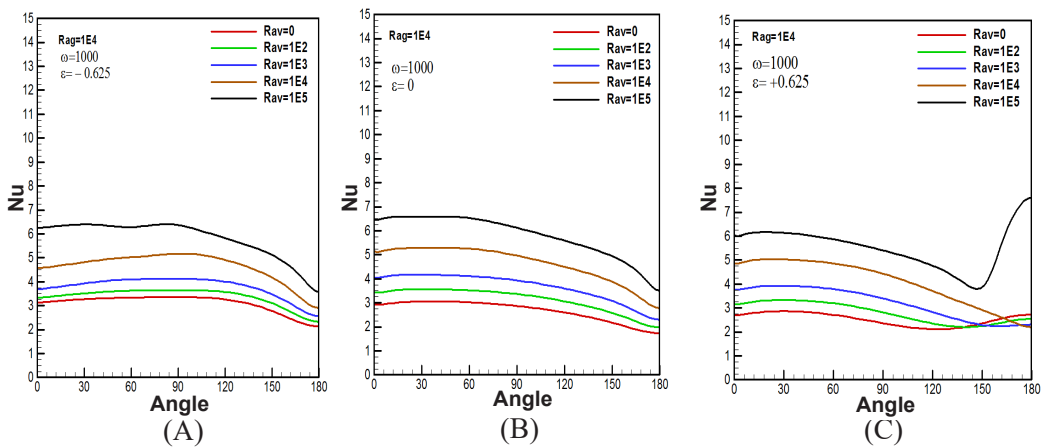


Figure 12. The local Nusselt number along the inner cylinder, $Ra = 10^4$, $Ra_{vib} = 10^5$ vibrational frequency $\omega = 1000$, $(r_o/r_i) = 2.6$ but in different eccentricities (A) $\epsilon = -0.625$, (B) $\epsilon = 0$, and (D) $\epsilon = +0.625$, respectively.

The Effect of Rayleigh Number Ra

The effect of Rayleigh number Ra on the local Nusselt number Nu with the circumferential position around the inner cylinder at various angles without and with the vibrational vibrated frequency ($\omega = 1000$) at eccentricity $\epsilon = (-0.625$ and $+0.625)$ is plotted at $Ra = (10^2, 10^3, 10^4, 10^5, \text{ and } 10^6)$ with $0 \leq Ra_{vib} \leq 10^5$ at each value of Ra Figures 13 and 14 (A–E). As the inner cylinder at the bottom $\epsilon = -0.625$, the Nu at $Ra = 10^2, 10^3$ and 10^4 does not change significantly and has an almost constant value for $0 \leq Ra_{vib} \leq 10^5$. Figures 13 and 14 show the proportional relation between the local Nusselt number and the vibrational Rayleigh

numbers, which increase as the Ra_{vib} increases at each Ra . It can be inferred that where the boundary layer starts to develop, heat transfer will become approximately without any remarkable variation. With increasing Rayleigh for each vibrational Rayleigh number $0 \leq Ra_{vib} \leq 10^5$, the local Nusselt numbers converge, close with each other, and increase rapidly, particularly at $Ra = 10^5$ and 10^6 — the optimal heat transfer rate at $Ra = 10^6$. The gradient of isotherms on the bottom wall increases rapidly when the inner cylinder keeps moving downward, and the gap between the inner cylinder and the bottom decreases, as shown in Figure 13. It may be ascribed to the secondary flow superimposed, leading to a higher heat transfer coefficient. As explained above from the streamlines and isotherms, at the positive vertical position $\epsilon = +0.625$, the Nu in the region ($0 \leq \phi \leq 90^\circ$) has a similar distribution to that at the inner cylinder at the bottom of the outer cylinder $\epsilon = -0.625$ is not significant for all different values of Rayleigh number. For all ranges of vibrational Rayleigh number, the symmetry on Nu is broken, and the deflection occurs, which causes a decrease in heat transfer rate at the angular location that deviates ($\phi > 90^\circ$). On the contrary, as Rayleigh increases to $Ra = 10^5$ and 10^6 , vibration enhances heat transfer and promotes breaking down the boundary layer. This improvement appears more pronounced at the high Rayleigh number.

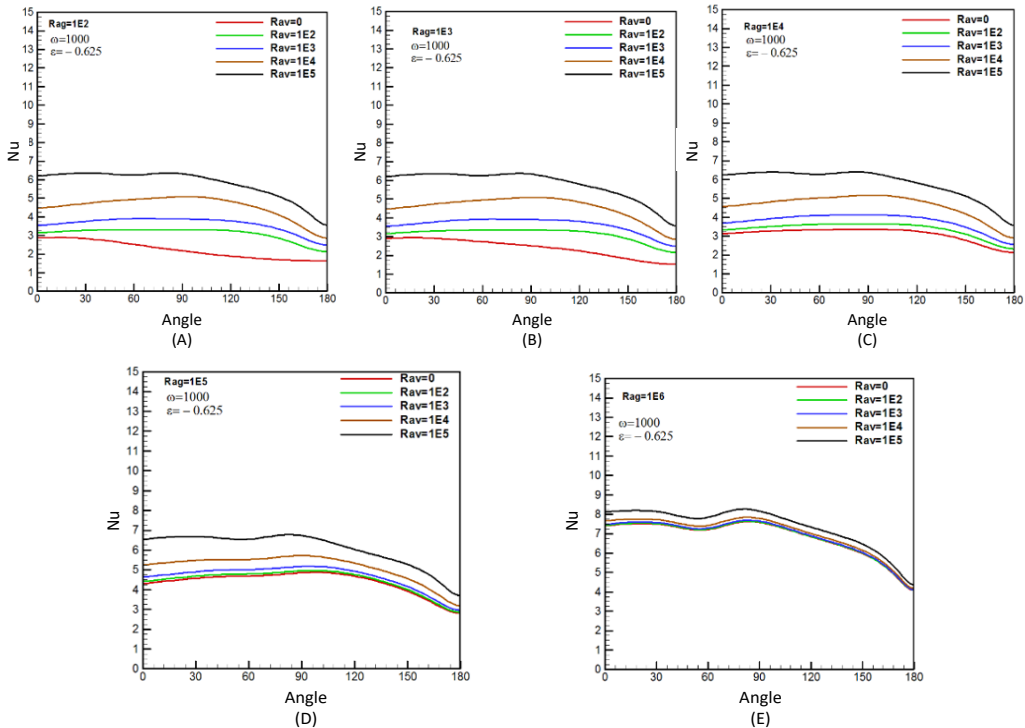


Figure 13. The local Nusselt number along the inner cylinder of annuli for the eccentricity $\epsilon = -0.62$; vibrational frequency $\omega = 1000$, $0 \leq Ra_{vib} \leq 10^5$, at different $Ra =$ (A) 10^2 , (B) 10^3 , (C) 10^4 , (D) 10^5 , (E) 10^6 , respectively.

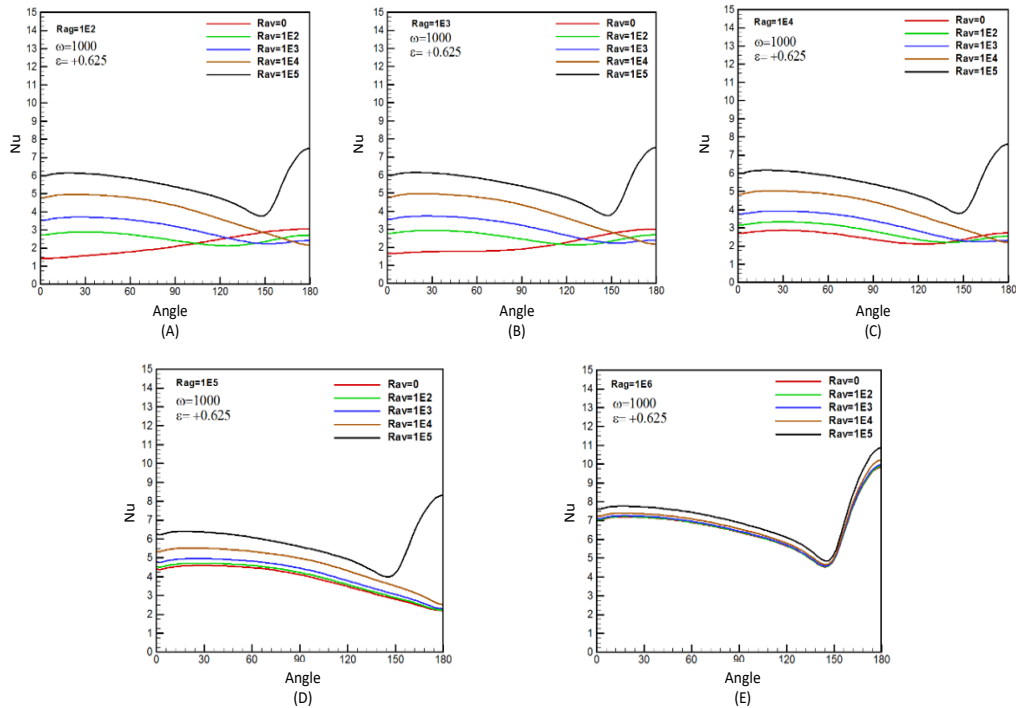


Figure 14. The local Nusselt number along the inner cylinder of annuli for the eccentricity $\epsilon = +0.625$; vibrational frequency $\omega = 1000$, $0 \leq Ra_{vib} \leq 105$, $Pr = 0.7$, $\frac{ro}{ri} = 2.6$ and $\frac{L}{Di} = 0.8$ at different $Ra =$ (A) 10^2 , (B) 10^3 , (C) 10^4 , (D) 10^5 , (E) 10^6 , respectively.

The Effect of Vibrational Frequency

Figures 15 and 16 show the effect of vibrational frequency ω on the local Nusselt number Nu with the circumferential position around the inner cylinder at various angles without and with the vibration at the vibrational frequency $\omega = (0, 100, 1000, \text{ and } 10000)$, eccentricity $\epsilon = (-0.625 \text{ and } +0.625)$ is plotted at $Ra = 10^4$, $Ra_{vib} = 10^5$. As can be seen, a significant effect of the frequency of the inner cylinder. The values of the local Nusselt number increased as ω increased very rapidly, especially for high vibrated frequency ($\omega = 10000$). The vibration effect appears more pronounced on the positive vertical position at $\epsilon = +0.625$ as it breaks down the boundary layer and enhances the heat transfer rate. Regardless of the status of the vibrated inner cylinder, it was evident that the thermal boundary layer became distorted due to vibration. This disturbance of the thermal boundary layer augments the local Nusselt number and, thus, the average Nusselt number. Consequently, replenishment, caused by vibrations in the inner cylinder, can be explained by comparing it to the separation of boundary layers that reduces local Nusselt numbers. Meanwhile, pressing makes the hot surface contact the fresher and colder fluid. As a result, the local Nusselt number rises.

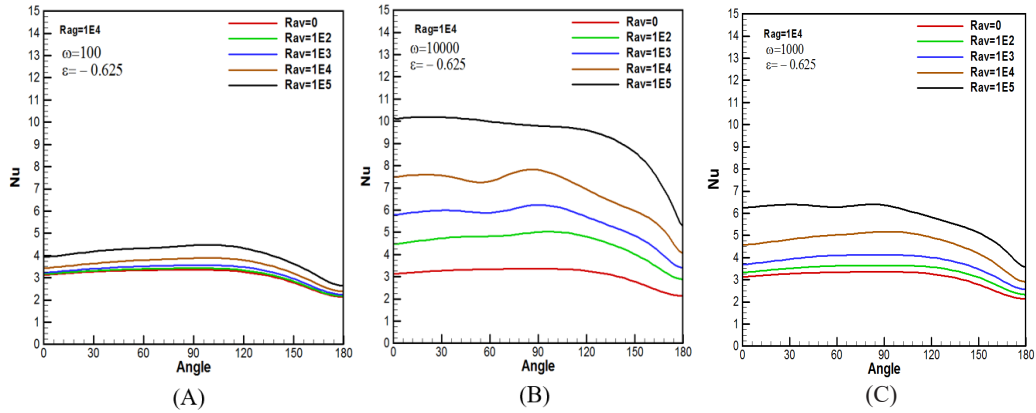


Figure 15. Local Nusselt number along the inner cylinder of annuli of the eccentricity $\epsilon = -0.625$, $Ra_L = 10^4$, $Ra_y = 10^5$ but in different vibrational frequencies (A) $\varpi = 100$, (B) $\varpi = 1000$, and (C) $\varpi = 10000$, respectively.

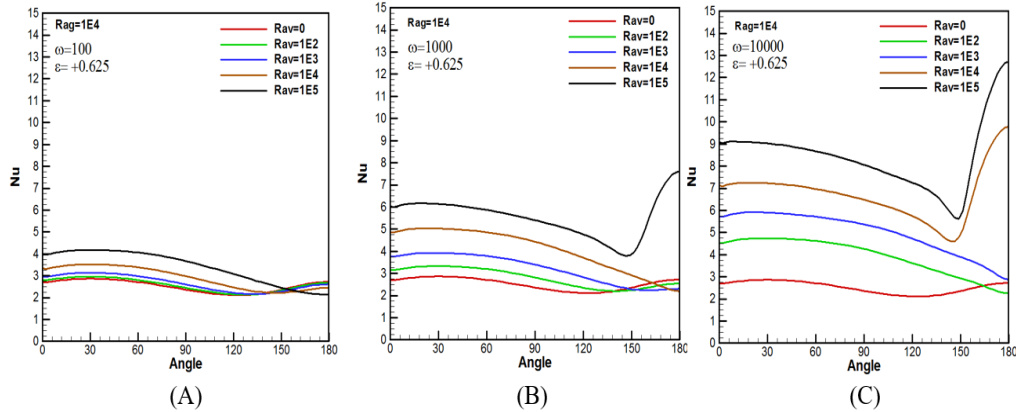


Figure 16. Local Nusselt numbers along the inner cylinder of annuli of the eccentricity $\epsilon = +0.625$, $Ra_L = 10^4$, $Ra_y = 10^5$ but in different vibrational frequencies (A) $\varpi = 100$, (B) $\varpi = 1000$, and (C) $\varpi = 10000$, respectively.

Average Nusselt Number (\overline{Nu})

The effect of vibrational frequency $\varpi = (100, 1000, \text{ and } 10000)$ on the eccentric configuration of the inner cylinder $\epsilon = (-0.625, -0.333, 0, +0.333 \text{ and } +0.625)$ at a range of the Rayleigh number $Ra = (10^2, 10^3, 10^4, 10^5, \text{ and } 10^6)$ on the average Nusselt number (\overline{Nu}) with a logarithmic vibrational Rayleigh number $0 \leq Ra_{vib} \leq 10^5$, is plotted in Figures 17 and 18 (A, B & C), respectively. In general, it is inferred from Figures 17 and 18 the following facts:

1. The average Nusselt number (\overline{Nu}) values increase with increasing Ra . Moreover, these values of (\overline{Nu}) converge and get closer to each other for all eccentric configurations at $Ra \geq 10^4$. The influence of the vibration reduces as the Rayleigh number increases $Ra \geq 10^5$.

2. The Nusselt number reaches its maximum value when the eccentricity of the inner cylinder is minimal (at a negative vertical position $\epsilon = -0.625$), while the minimum is when the inner cylinder's eccentricity is maximal at ($\epsilon = +0.625$). When the inner cylinder moves upward at ($\epsilon = +0.625$), the conduction mode of the heat transfer zone at the bottom region is expanded, increasing the thermal resistance in the annulus. On the other hand, when the eccentricity of the inner cylinder reaches its minimum value at ($\epsilon = -0.625$), the convection mode of the heat transfer zone at the top region is expanded, and the conduction is dominated mode zone at the bottom area is reduced. The two actions reduce the annulus's heat flow resistance (thermal boundary layer). Figure 19 shows the average Nusselt number (\overline{Nu}) with a logarithmic vibrational Rayleigh number at different eccentricities.
3. Figures 17 and 18 show the effect of the vibrational frequency of the inner cylinder on the average Nusselt number (\overline{Nu}). Figures 17 and 18 show that when the inner cylinder is at the bottom region, the heat flow is greatly increased, but the heat flow is significantly decreased when the inner cylinder is at the top region. A high vibrational frequency of the inner cylinder further decreases the thermal resistance at the top region and increases the resistance at the bottom region even more.

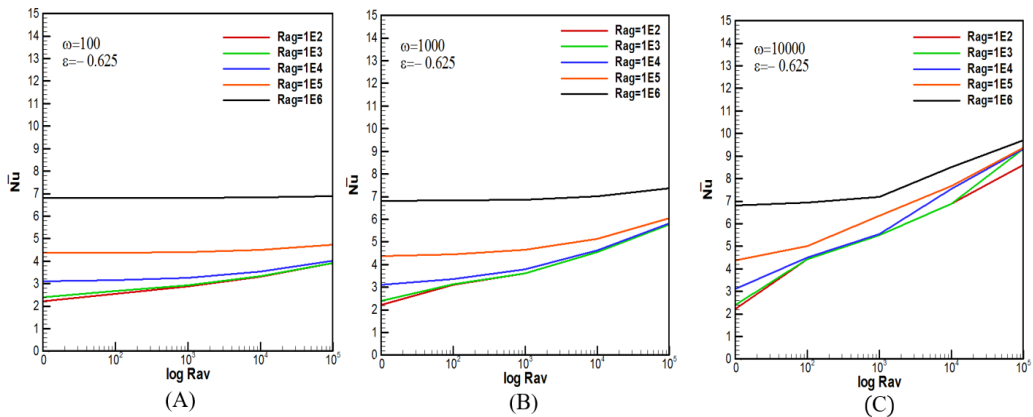


Figure 17. Average Nusselt numbers versus $\log Ra_v$, of annuli of the eccentricity $\epsilon = -0.625$; $10^2 \leq Ra \leq 10^6$, at (A) $\omega = 100$, (B) $\omega = 1000$, and (C) $\omega = 10000$, respectively.

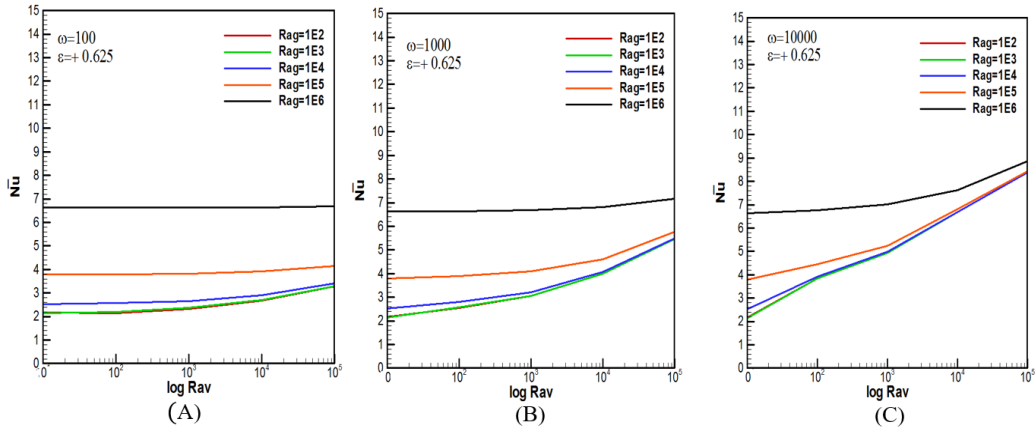


Figure 18. Average Nusselt numbers versus $\log Ra_v$ of annuli of the eccentricity $\epsilon = +0.625$; $10^2 \leq Ra \leq 10^6$, (A) $\omega = 100$, (B) $\omega = 1000$, and (C) $\omega = 10000$, respectively.

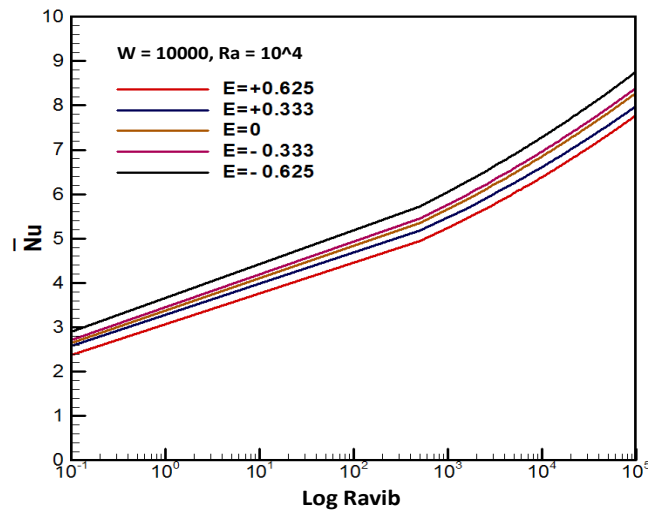


Figure 19. Average Nusselt numbers versus $\log Ra_v$ along the inner cylinder at $Ra = 10^4$, $0 \leq Ra_{vib} \leq 10^5$, vibrational frequency $\omega = 1000$, but in different eccentricity.

Table 4

Enhancement factor at $\epsilon = +0.625$

(a) $\omega = 100$					
Ra_{vib}	$Ra = 10^2$	$Ra = 10^3$	$Ra = 10^4$	$Ra = 10^5$	$Ra = 10^6$
0	1	1	1	1.000	1.000
100	0.986	1.027	1.019	1.003	1.000
1000	1.065	1.103	1.058	1.0111	1.001

Table 4 (Continue)

(a) $\Omega = 100$					
Ra_{vib}	$Ra = 10^2$	$Ra = 10^3$	$Ra = 10^4$	$Ra = 10^5$	$Ra = 10^6$
0	1	1	1	1.000	1.000
100	0.986	1.027	1.019	1.003	1.000
1000	1.065	1.103	1.058	1.0111	1.001
10000	1.233	1.266	1.153	1.034	1.003
100000	1.508	1.541	1.353	1.098	1.010
(b) $\Omega = 1000$					
Ra_{vib}	$Ra = 10^2$	$Ra = 10^3$	$Ra = 10^4$	$Ra = 10^5$	$Ra = 10^6$
0	1	1	1	1	1
100	1.166	1.200	1.109	1.027	1.002
1000	1.401	1.433	1.272	1.081	1.009
10000	1.833	1.870	1.619	1.213	1.028
100000	2.515	2.561	2.188	1.526	1.081
(c) $\Omega = 10000$					
Ra_{vib}	$Ra = 10^2$	$Ra = 10^3$	$Ra = 10^4$	$Ra = 10^5$	$Ra = 10^6$
0	1	1	1	1	1
100	1.767	1.802	1.558	1.175	1.020
1000	2.275	2.312	1.980	1.382	1.058
10000	3.068	3.123	2.658	1.795	1.1521
100000	3.855	3.924	3.336	2.229	1.339

Table 5

Enhancement factor at $\epsilon = - 0.625$

(a) $\Omega = 100$					
Ra_{vib}	$Ra = 10^2$	$Ra = 10^3$	$Ra = 10^4$	$Ra = 10^5$	$Ra = 10^6$
0	1	1	1	1	1
100	1.1498	1.114	1.018	1.002	1
1000	1.293	1.222	1.054	1.009	1.001
10000	1.488	1.389	1.138	1.027	1.003
100000	1.763	1.638	1.300	1.080	1.010
(b) $\Omega = 1000$					
Ra_{vib}	$Ra = 10^2$	$Ra = 10^3$	$Ra = 10^4$	$Ra = 10^5$	$Ra = 10^6$
0	1	1	1	1	1

Table 5 (Continue)

(b) $\omega = 1000$					
Ra_{vib}	$Ra = 10^2$	$Ra = 10^3$	$Ra = 10^4$	$Ra = 10^5$	$Ra = 10^6$
0	1	1	1	1	1
100	1.397	1.307	1.089	1.021	1.002
1000	1.626	1.514	1.221	1.064	1.009
10000	2.050	1.903	1.494	1.173	1.028
100000	2.605	2.415	1.876	1.386	1.082

(c) $\omega = 10000$					
Ra_{vib}	$Ra = 10^2$	$Ra = 10^3$	$Ra = 10^4$	$Ra = 10^5$	$Ra = 10^6$
0	1	1	1	1	1
100	1.995	1.851	1.452	1.144	1.019
1000	2.478	2.298	1.786	1.451	1.058
10000	3.103	2.881	2.227	1.755	1.251
100000	3.883	3.894	3.012	2.142	1.424

Enhancement Factor (E)

The enhancement factor for the heat transfer enhancement by an external oscillation is defined as Equation 23 (Kim et al., 2002).

$$E (\overline{Nu}) = \frac{(\overline{Nu})_p}{(\overline{Nu})_s} \tag{23}$$

Enhancement factor (E) is the average Nusselt number with a vibration ratio to the steady-state average Nusselt number. For each Rayleigh number, the percentage of increase in average Nusselt numbers for frequency is tabulated in Tables 3 and 4. It is shown that an increase in vibrational levels increases the enhancement factor but decreases with the fall of vibration levels.

Suggested Correlation

The present study calculates the relationship between the average Nusselt number (\overline{Nu}), Rayleigh number, and the vibrational Rayleigh number made using these parameters. Based on that and the inner cylinder position (eccentricity ratio) (ϵ), It was shown that the heat transfer equations for all the parts and vibrating the inner cylinder have the same following form (Equation 24):

$$\overline{Nu} = C * (Ra)^A * (Ra_{vib})^B \tag{24}$$

As a result, Table 6 lists all the constant values (A, B, and C) that appear in the equation for each position based on the search criteria. Figure 20 shows the relation between the Nusselt number calculated from the suggested equations (\overline{Nu}_c) and the numerical one (\overline{Nu}). It is seen from Figure 20 that most of the numerical Nusselt number points fall within $\pm 13.7\%$ of the predicted Nusselt number.

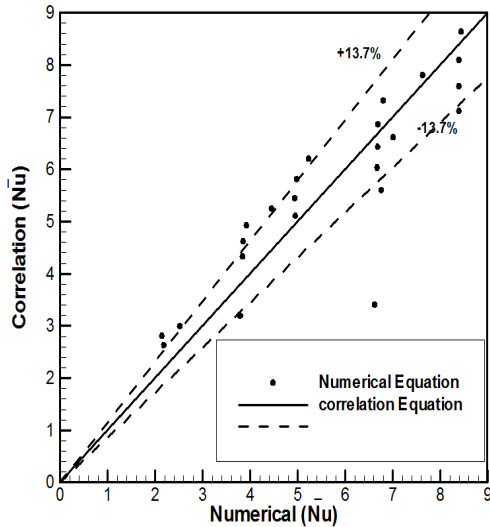


Table 6
Values of constants (A, B, and C)

ϵ	ω	A	B	C
- 0.625	100	1.356	0.107	0.01
	1000	2.076	0.067	0.03
	10000	2.076	0.03	0.071
0	100	1.017	0.126	0.013
	1000	1.86	0.069	0.038
	10000	2.959	0.026	0.065
+ 0.625	100	0.914	0.135	0.08
	1000	2.133	0.069	0.016
	10000	2.732	0.028	0.072

Figure 20. The predicted (\overline{Nu}) results

CONCLUSION

A study of vibration and natural heat convection in an annular circle was conducted between two horizontally centric and vertically eccentric long cylinders during gravity and vibration. The body-fitted coordinate system (BFCs) transformed the physical field into a rectangular domain. Finite-difference schemes approximate partial differential equations directly using iterative methods. From this study, it is concluded that:

1. It was revealed that vibration boosted the heat transfer rate at which the flow transitioned from laminar to turbulent. This turbulence occurred due to a disruption in the flow produced by the generated vibration. Many factors influence the Nusselt number, including the following:
 - a. For each inner cylinder location, the Nusselt number increases as the vibration frequency increases.
 - b. The heat transfer rate increased significantly for the negative vertical position at ($\epsilon = -0.625$) for the same frequency and Rayleigh number compared with the positive vertical position ($\epsilon = +0.625$).

- c. The heat transfer rate decreased for the same inner cylinder position, and vibrational frequency as the Rayleigh number decreased in the annulus and significantly increased as the Rayleigh number increased.
2. The Rayleigh number, vibrational number, frequency, and inner cylinder locations were all associated with the average Nusselt number.

ACKNOWLEDGEMENT

The authors appreciate the cooperation of the University of Technology/Iraq in completing this work.

NOMENCLATURE

Parameter	Symbol
Di, Do	Inner and outer cylinder diameter (m)
e	Eccentricity(m)
ϵ	Dimensionless eccentricity = $\frac{e}{L}$
g	Gravitational acceleration ($\frac{m}{s^2}$)
L	The gap width(radius difference) = (Ro-Ri) m
h	Heat transfer coefficient W/m ² .K
k	Thermal conductivity(W/m.°C)
J	Jacobian of coordinate transformation
U, V	Dimensionless horizontal and vertical components of velocity
Nu, Nu	Local and average Nusselt number
Pr	Prandtle number ($\frac{\nu}{\alpha}$)
q''	Heat flux ($\frac{W}{m^2}$)
Gr	Grashof number ($g\beta qL^4/K\vartheta^2$)
Ra_L	Rayleigh number ($g\beta qL^4/K\vartheta^2$)Pr
Gr_{vib}	Vibrational Grashof number = $\frac{1}{2} \left[\frac{\rho^2 (b\Omega)\beta q L^2}{K \mu^2} \right]^2$
Ra_{vib}	Vibrational Rayleigh number $\left(\frac{1}{2} [\rho^2 (b\Omega)\beta q L^2 / K \mu^2]^2 Pr \right)$
θ	Dimensionless temperature ($\frac{(T-T_c)K}{q''L}$) in the case of CHF
(ξ, η)	Bipolar coordinate in the computational domain

REFERENCES

- Alawadhi, E. M. (2008). Natural convection flow in a horizontal annulus with an oscillating inner cylinder using Lagrangian–Eulerian kinematics. *Computers & Fluids*, 37, 1253-1261.
- Al-Azzawi, M. M., Abdullah, A. R., Majel, B. M., & Habeeb, L. J. (2021). Experimental investigation of the effect of forced vibration on natural convection heat transfer in a concentric vertical cylinder. *Journal of Mechanical Engineering Research and Developments*, 44(3), 56-65.
- Ali, M., Rad, M. M., Nuhait, A., Almuzaiqer, R., Alimoradi, A., & Tlili, I. (2020). New equations for Nusselt number and friction factor of the annulus side of the conically coiled tubes in tube heat exchangers. *Applied Thermal Engineering*, 164, Article 114545. <https://doi.org/10.1016/j.applthermaleng.2019.114545>
- Bouzerzour, A., Tayebi, T., Chamkha, A. J., & Djeddar, M. (2020). Numerical investigation of natural convection nanofluid flow in an annular space between confocal elliptic cylinders at various geometrical orientations. *Computational Thermal Sciences: An International Journal*, 12(2), 99-114. <https://doi.org/10.1615/computthermalsci.2020026938>
- Fu, W. S., & Huang, C. P. (2006). Effects of a vibrational heat surface on natural convection in a vertical channel flow. *International Journal of Heat and Mass Transfer*, 49(7-8), 1340-1349. <https://doi.org/10.1016/j.ijheatmasstransfer.2005.10.028>
- Ho, C. J., Lin, Y. H., & Chen, T. C., (1989). A numerical study of natural convection in concentric and eccentric horizontal cylindrical annuli with mixed boundary conditions. *International Journal of Heat and Fluid Flow*, 10(1), 40-47. [https://doi.org/10.1016/0142-727X\(89\)90053-2](https://doi.org/10.1016/0142-727X(89)90053-2)
- Hosseini, A., Meghdadi I. A. H., & Shirani, E. (2018). Experimental investigation of surface vibration effects on increasing the stability and heat transfer coefficient of MWCNTs-water nanofluid in a flexible double pipe heat exchanger. *Experimental Thermal and Fluid Science*, 90, 275-285. <https://doi.org/10.1016/j.expthermflusci.2017.09.018>
- Intiaz, H., & Mahfouz, F. M. (2017). Conjugated conduction-free convection heat transfer in an annulus heated at either constant wall temperature or constant heat flux. *Journal of Engineering and Technology*, 36(2), 273-288. <https://doi.org/10.22581/muet1982.1702.06>
- Kim, S. K., Kim, S. Y., & Choi, Y. D. (2002). Resonance of natural convection in a side heated enclosure with a mechanically oscillating bottom wall. *International Journal of Heat and Mass Transfer*, 45(15), 3155-3162. [https://doi.org/10.1016/S0017-9310\(02\)00030-3](https://doi.org/10.1016/S0017-9310(02)00030-3)
- Kuehn, T. H., & Goldstein, R. J. (1976). An experimental and theoretical study of natural convection in the annulus between horizontal concentric cylinders. *Journal of Fluid mechanics*, 74(4), 695-719. <https://doi.org/10.1017/S0022112076002012>
- Kuehn, T. H., & Goldstein, R. J. (1978). An experimental study of natural convection heat transfer in concentric and eccentric horizontal cylindrical annuli. *Journal of Heat and Mass Transfer*, 100(4), 635-640. <https://doi.org/10.1115/1.3450869>
- Liu, W., Yang, Z., Zhang, B., & Lv, P. (2017). Experimental study on the effects of mechanical vibration on the heat transfer characteristics of tubular laminar flow. *International Journal of Heat and Mass Transfer*, 115, 169-179. <https://doi.org/10.1016/j.ijheatmasstransfer.2017.07.025>

- Mahfouz, F. M. (2012). Heat convection within an eccentric annulus heated at either constant wall temperature or constant heat flux. *Journal of Heat Transfer*, *134*(8), Article 082502. <https://doi.org/10.1115/1.4006170>
- Mahian, O., Pop, I., Sahin, A. Z., Oztop, H. F., & Wongwises, S. (2013). Irreversibility analysis of a vertical annulus using TiO₂/water nanofluid with MHD flow effects. *International Journal of Heat and Mass Transfer*, *64*, 671-679. <https://doi.org/10.1016/j.ijheatmasstransfer.2013.05.001>
- Nasrat, K. M., Hameed, D. L., & Sadiq, E. A. (2019). The effect of transverse vibration on the natural convection heat transfer in a rectangular enclosure. *International Journal of Mechanical Engineering and Technology*, *10*(6), 266-277.
- Projahn, U., Rieger, H., & Beer, H. (1981). Numerical analysis of laminar natural convection between concentric and eccentric cylinders. *Numerical Heat Transfer*, *4*(2), 131-146. <https://doi.org/10.1080/01495728108961783>
- Sarhan, A. R., Karim, M. R., Kadhim, Z. K., & Naser, J. (2019). Experimental investigation on the effect of vertical vibration on thermal performances of rectangular flat plate. *Experimental Thermal and Fluid Science*, *101*, 231-240. <https://doi.org/10.1016/j.expthermflusci.2018.10.024>
- Shahsavari, A., Moradi, M., & Bahiraei, M. (2018). Heat transfer and entropy generation optimization for flow of a non-Newtonian hybrid nanofluid containing coated CNT/Fe₃O₄ nanoparticles in a concentric annulus. *Journal of the Taiwan Institute of Chemical Engineers*, *84*, 28-40. <https://doi.org/10.1016/j.jtice.2017.12.029>
- Shokouhmand, H., Abadi, S. M. A. N. R., & Jafari, A. (2011). The effect of the horizontal vibrations on natural heat transfer from an isothermal array of cylinders. *International Journal of Mechanics and Materials in Design*, *7*(4), 313-326. <https://doi.org/10.1007/s10999-011-9170-6>
- Tayebi, T., & Chamkha, A. J. (2021). Analysis of the effects of local thermal non-equilibrium (LTNE) on thermo-natural convection in an elliptical annular space separated by a nanofluid-saturated porous sleeve. *International Communications in Heat and Mass Transfer*, *129*, Article 105725. <https://doi.org/10.1016/j.icheatmasstransfer.2021.105725>
- Tayebi, T., Chamkha, A. J., Melaibari, A. A., & Raouache, E. (2021). Effect of internal heat generation or absorption on conjugate thermal-free convection of a suspension of hybrid nanofluid in a partitioned circular annulus. *Communications in Heat and Mass Transfer*, *126*, Article 105397. <https://doi.org/10.1016/j.icheatmasstransfer.2021.105397>
- Tayebi, T., Chamkha, A. J., Öztop, H. F., & Bouzeroura, L. (2022). Local thermal non-equilibrium (LTNE) effects on thermal-free convection in a nanofluid-saturated horizontal elliptical non-Darcian porous annulus. *Mathematics and Computers in Simulation*, *194*, 124-140. <https://doi.org/10.1016/j.matcom.2021.11.011>
- Tayebi, T., Djeddar, M., Bouzerzour, A., Azzouz, K., & Khan, Z. H. (2016). Numerical Simulation of Natural Convection of Water Based Nanofluids in Horizontal Eccentric Cylindrical Annuli. *Journal of Nanofluids*, *5*(2), 253-263. <https://doi.org/10.1166/jon.2016.1211>
- Tayebi, T., Öztop, H. F., & Chamkha, A. J. (2021). MHD natural convection of a CNT-based nanofluid-filled annular circular enclosure with inner heat-generating solid cylinder. *The European Physical Journal Plus*, *136*(2), Article 150. <https://doi.org/10.1140/epjp/s13360-021-01106-7>

- Thompson, J., F., Thames, F. C., & Mastin, C. W. (1974). Automatic numerical generation of body-fitted curvilinear coordinate system for fields containing any number of arbitrary two-dimensional bodies. *Journal of Computational Physics*, 15(3), 299-319.
- Wang, B. F., Zhou, Q., & Sun, C. (2020). *Vibration-Induced Boundary-Layer Destabilization Achieves Massive Heat-Transport Enhancement*. *Science Advances*, 6(21). <https://doi.org/10.1126/sciadv.aaz8239>